Article

Modeling Short-Range Order in Disordered Rocksalt Cathodes by Pair Distribution Function Analysis

Nathan J. Szymanski, Zhengyan Lun, Jue Liu, Ethan C. Self, Christopher J. Bartel, Jagjit Nanda, Bin Ouyang,* and Gerbrand Ceder*

ACCESS | 📊 Metrics & More | 📖 Article Recommendations | 🅢 Supporting Information

ABSTRACT: Pair distribution function (PDF) analysis is a powerful technique for the characterization of short-range order (SRO) in disordered materials. Accurate interpretation of experimental PDF data is critically reliant on the development of structural models that can account for local variations in site occupancies and bond lengths. To this end, we outline an approach to model SRO using first-principles calculations based on the cluster-expansion formalism. These methods are validated on neutron scattering data from two disordered rocksalt oxyfluorides, $Li_{1.3}Mn_{0.4}Ti_{0.3}O_{1.7}F_{0.3}$ and $Li_{1.3}Mn_{0.4}Nb_{0.2}Ti_{0.1}O_{1.7}F_{0.3}$. For each composition, we demonstrate that an average structure without any SRO fails to reproduce several key features in the experimental PDF. To pinpoint the origin of the suspected SRO in these materials, configurational and displacive effects were separately investigated using two disparate models. Special quasi-random structures were relaxed using density functional theory to account for local changes in bond lengths while maintaining a near-random ionic configuration. This leads to slightly improved accuracy but still misrepresents asymmetry in the first few peaks of the PDF. Monte Carlo simulations were performed to model configurational SRO on a fixed lattice, which by itself is shown to have a minimal influence on the PDF. Instead, we find that it is the bond length relaxations within environments created by SRO which controls the details of the PDF, thereby highlighting the subtle but important coupling between configurational and displacive SRO in disordered materials.
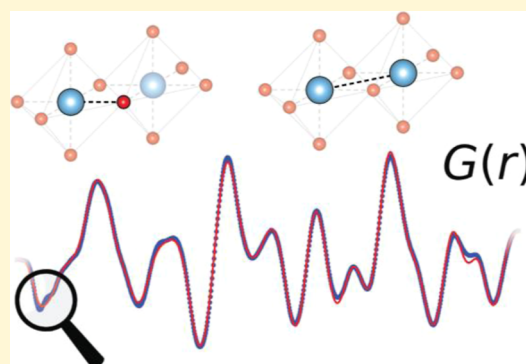
INTRODUCTION

Disordered crystalline materials play a vital role in modern technology, finding use in a wide range of applications, including Li-ion cathodes, hard coatings,[1] and high-temperature superconductors.[2] Such materials are characterized by a nominally random arrangement of ionic species distributed across the sites of a periodic structure. Yet, disordered crystals often possess some degree of chemical short-range order (SRO), whereby the occupancies and positions of individual species are correlated with one another.[3] Cu_3Au is a well-studied example of this property as previous work has shown that SRO favors increased Cu–Au coordination relative to a completely random alloy.[4,5] Similar effects have also been reported in more complex systems such as disordered rocksalt (DRX) oxyfluorides $(Li_{1+x}TM_{1−x}O_{2−y}F_y)$, where calculations predict that Li–F bonds are strongly preferred over TM–F bonds (for TM = 3d transition metals).[6,7] Importantly, these factors can have a significant influence on the properties of disordered materials. For example, the correlation between Li and F modifies the diffusion network in DRX oxyfluorides, thus affecting their rate performance when used as Li-ion cathodes.[8–10] To enable the use of SRO as an effective handle for the optimization of disordered materials, a reliable technique for its characterization is needed. While historically diffuse scattering on single crystals has been used to quantify SRO in binary alloys,[11–13] this technique is less applicable to the powder form of many technologically relevant oxides. Analysis of the pair distribution function (PDF) is therefore considered to handle such cases.

PDF measurements are performed by detecting the intensity of high-energy X-rays, neutrons, or electrons scattered from a sample at various angles.[14] These are similar to conventional diffraction experiments, except that PDF analysis makes use of the entire spectrum, including both Bragg and diffuse scattering. Whereas Bragg peaks are related to a long-range order (LRO) in the average structure, the inspection of the diffuse scattering can provide information regarding the local structure.[15] Through a Fourier transform of the total spectrum, the PDF gives a real-space representation that describes the probability of finding a pair of atoms separated by a distance (r).[16] Structural models may then be refined to fit this data and

provide a quantitative description of SRO. In contrast to the refinement of structures based on conventional diffraction data, where only primitive unit cells are typically considered (e.g., using the methods of Rietveld,[17] Pawley,[18] or Le Bail[19]), modeling PDF data often requires the use of large supercells to account for the wide range of coordination environments that may exist.[20] This so-called "large box" approach has been successfully applied to study SRO in many disordered materials such as Cu_3Au[4] and $Ca_xSr_{1-x}TiO_3$,[21,22] but it becomes less tractable for complex, multi-component systems including high-entropy alloys and DRX cathodes. Such cases introduce an exceedingly large number of variables and are therefore prone to overfitting experimental data. While many different structural models can reproduce a single PDF, not all will accurately describe the positions and occupancies of distinct sites within the corresponding material.[23−25]

To generate structural models that are likely to provide an accurate representation of experimental materials, first-principles calculations may be used to filter such models by their free energy. In particular, the cluster-expansion (CE) formalism provides an effective method to model the configurational thermodynamics of disordered systems.[26] By coupling this approach with Monte Carlo (MC) simulations, low-energy configurations can be sampled and subsequently relaxed using density functional theory (DFT).[27] Structures generated from these methods have been shown to accurately reproduce experimental PDF data from several disordered battery materials.[6,9] Here, we build upon previous work by detailing the relationship between SRO and peak asymmetries (or lack thereof) in experimental PDFs, which are modeled in a quantitative fashion using first-principles calculations. We also demonstrate how these models can be used to disentangle (1) configurational SRO, as related to correlations between site occupancies, and (2) displacive SRO which is related to local changes in bond lengths associated with distinct coordination environments.[28]

The methods presented herein are validated on neutron scattering data obtained from two DRX oxyfluorides: $Li_{1.3}Mn_{0.4}Ti_{0.3}O_{1.7}F_{0.3}$ (LMTOF) and $Li_{1.3}Mn_{0.4}Nb_{0.2}Ti_{0.1}O_{1.7}F_{0.3}$ (LMNTOF). These compositions are of interest for their use as Li-ion cathodes, where Mn provides high redox capacity with good reversibility and low cost.[29] Ti and Nb are included as d^0 cations (Ti^{4+} and Nb^{5+}) which stabilize the disordered structures by accommodating local strain.[30,31] Partial substitution of O with F is considered to improve the cyclability of these cathodes, and F is also of interest for its modification of SRO as it preferentially bonds with Li.[8] To refine the structure of each composition using the neutron PDF, we start with an average structure containing a random configuration of ions on a fixed fcc lattice. While this model provides a good fit of the conventional diffraction pattern for each material, it fails to accurately reproduce the first few peaks of the PDF. Displacive SRO is probed using special quasi-random structures (SQSs) which closely replicate a random configuration of ions within a finite supercell. By relaxing these structures with DFT, we account for local changes in the bond lengths caused by ionic size mismatches and Jahn−Teller distortions around Mn^{3+}. Although this leads to improved agreement with the experimental data, the shapes of several peaks at low distances are still poorly modeled. To further improve the accuracy of the simulated PDF, configurational SRO is modeled using low-energy structures sampled from the MC simulations. We find that configurational SRO

itself has little direct influence on the PDF of each material studied in this work; however, it has a significant indirect influence on the PDF by setting the local coordination environments and therefore controlling the displacements that take place. For example, cation−anion correlations are shown to dictate the strength of Jahn−Teller distortions in materials containing Mn^{3+}, whereas cation−cation correlations govern local relaxations associated with the electrostatic repulsion between high-valent ions such as Ti^{4+} and Nb^{5+}. These findings highlight the utility of PDF analysis as applied to disordered crystalline materials and provide a blueprint for studying SRO in multi-component systems using first-principles simulations.

■ METHODS

Materials Synthesis. LMTOF and LMNTOF were synthesized using a traditional solid-state method. Li_2CO_3 (Sigma-Aldrich, 99%), MnO (Alfa Aesar, 99%), Mn_2O_3 (Alfa Aesar, 99.9%), TiO_2 (Alfa Aesar, 99.9%), Nb_2O_5 (Sigma-Aldrich, 99.99%), and LiF (Alfa Aesar, 99.99%) were used as precursors. Li_2CO_3 and LiF were both purchased with enriched ^7Li content (≥99 at. %). For each target, the precursors were stoichiometrically mixed in ethanol with a Retsch PM 400 planetary ball mill at a rate of 180 rpm for 12 h. An excess weight of ∼12% was included for Li_2CO_3 to compensate for volatility at high temperatures. The mixed precursors were dried in an oven at 70 °C overnight and subsequently pelletized. The pellets were sintered at 1000° C under an Ar atmosphere for 4 h, followed by a fast cooling to room temperature under the same atmosphere. The resulting products were transferred to a glovebox and ground into fine powders for later characterization.

Neutron Diffraction. Neutron time-of-flight measurements were carried out using the Nanoscale-Ordered Materials Diffractometer (NOMAD, BL-1B) at the Spallation Neutron Source (SNS, Oak Ridge National Laboratory).[32,33] For both LMTOF and LMNTOF, 300 mg samples were sealed under Ar in thin walled 3 mm quartz capillaries, which were characterized at room temperature. Four 24 min scans (2C each) were collected and summed together to improve the statistics. The collected neutron diffraction data were background subtracted (using an empty quartz capillary) and normalized against the scattering from a 6 mm V rod. The reduced neutron PDF, $G(r)$, was calculated through a sine Fourier transform of the normalized scattering function, $S(Q)$, according to the following equation based on $Q_{max} = 35$ Å^{-1}

$$G(r) = r(1 - g(r)) = \frac{1}{2\pi^2\rho_0}\int_{Q_{min}}^{Q_{max}} Q(S(Q) - 1)\sin(Qr)dQ \quad (1)$$

Structure Refinement Based on the PDF. Refinement was performed with the diffpy-CMI package, a Python-based modeling framework for atomic-structure analysis using experimental scattering data.[34] For a given structure, the level of mismatch between the simulated (G_{calc}) and experimental PDF (G_{obs}) is quantified by

$$R_w = \sqrt{\frac{\sum_n (G_{obs,n} - G_{calc,n})^2}{\sum_n G_{obs,n}^2}} \quad (2)$$

where a large R_w value signifies a poor fit to the experimental data. Least-squares regression was used to minimize R_w over a range of 1.5−10.0 Å. This range was kept limited to focus on the features associated with SRO. Regression was carried out by varying the isotropic atomic displacement parameter (U_{iso}) of each species, including Li, Mn, Ti, Nb, O, and F. To avoid overfitting and ensure that the models were realistic, each parameter was bounded by 0.001 Å^2 ≤ U_{iso} ≤ 0.025 Å^2. The lattice constants of the simulated unit cells were constrained to their experimental values (4.15 Å for LMTOF and 4.22 Å for LMNTOF), which were determined based on the peak positions in each diffraction pattern. The scaling constant associated with each PDF was optimized freely. All remaining parameters (e.g.,

describing the background signal) were set to their default values within the diffpy-CMI package.

The magnitude of each peak in the neutron PDF is related to the coherent neutron scattering lengths of the elements in the corresponding sample. To model the PDFs in this work, we assume the following scattering lengths which are based on the most abundant isotope of each element in LMTOF and LMNTOF[35]

$$b_{Li} = -2.22 \text{ fm}, b_{Mn} = -3.73 \text{ fm}, b_{Ti} = -6.08 \text{ fm}, b_{Nb} = 7.054 \text{ fm}$$

$$b_O = 5.803 \text{ fm}, b_F = 5.656 \text{ fm}$$

Because large differences exist between the scattering lengths of the cations, they can in principle be distinguished by neutron PDF should the materials possess sufficiently strong configurational SRO. In contrast, O and F have very similar scattering lengths and therefore cannot easily be distinguished by inspecting the magnitude of each peak in the neutron PDF. However, we will show that the bonding preferences of O and F can still be determined since each anion affects its neighboring bond lengths differently. This in turn influences the shape and position of each peak in the PDF, which can be assessed to calculate the relative abundance of various bond pairs.

Average Structure. For disordered crystalline materials, refinement based on conventional diffraction data is typically performed using an average structural model based on the virtual crystal approximation.[36] This approach relies on the use of a primitive unit cell, wherein each site is occupied by a linear combination of the species comprising the net composition of the material. For example, the coherent neutron scattering length (b) associated with each site in the average structure of LMTOF is calculated as follows

$$b_{cation} = 0.65b_{Li} + 0.2b_{Mn} + 0.15b_{Ti} \tag{3}$$

$$b_{anion} = 0.85b_O + 0.15b_F \tag{4}$$

Because the sites within each sublattice share equal scattering lengths, this model represents a completely random configuration of ions without any configurational SRO. Moreover, all species occupy a fixed fcc lattice such that displacive SRO is neglected as well. The average structure therefore serves as a baseline from which a comparison can be made with more advanced models that include various aspects of SRO.

Cluster Expansion. A complete model for the configurational thermodynamics of DRX oxyfluorides must account for the distribution of Li and TMs on the cation sublattice as well as the O/F arrangement on the anion sublattice. For this task, we used the coupled cluster-expansion approach,[26] which has been demonstrated to accurately model the properties of several DRX oxyfluorides.[7,8,30,37] With this approach, the configurational dependence of the energy (E) is calculated by an expansion into different cluster functions as follows

$$E = \sum_{i,sp_1} J_i^{sp_1} \sigma_i^{sp_1} + \sum_{i,j,sp_1,sp_2} J_{ij}^{sp_1 sp_2} \sigma_i^{sp_1} \sigma_j^{sp_2} + ... \tag{5}$$

where σ_i^{sp} represents the occupancy of each site i with a certain species sp and J refers to the effective cluster interactions (ECIs). Here, we include pair interactions up to 7.1 Å, triplet interactions up to 4.0 Å, and quadruplet interactions up to 4.0 Å based on a primitive cell of the rocksalt structure with a lattice parameter of 3 Å. All interactions were taken with respect to a baseline screened electrostatic energy defined by the formal charges of the ionic species (Li$^+$, Mn^{2+}, Mn^{3+}, Ti^{4+}, Nb^{5+}, O^{2-}, and F$^-$). The ECIs were fitted to DFT-calculated energies from 6154 structures using L$_1$-regularized least-squares regression.[38]

With the established CE, canonical MC simulations were performed to sample low-energy ionic configurations for each DRX composition at temperatures of 1000 and 1500 °C using the Metropolis−Hastings algorithm.[39] To probe the influence of the simulated cell size on the fit to experimental PDF data, supercells were generated with dimensions of 4 × 5 × 5 (200 atoms), 4 × 5 × 6 (240 atoms), 4 × 5 × 8 (320 atoms), 5 × 5 × 8 (400 atoms), and 5 ×

6 × 8 (480 atoms). For each composition and cell size, the equilibration consisted of 2,000,000 MC steps and the production consisted of 8,000,000 MC steps. A total of 140 configurations were generated for each composition, and these structures provided starting points for the DFT calculations described in the next section.

As a comparison to the MC structures that account for configurational SRO, we also generated a SQS for each DRX composition. These are periodic structures whose occupancies are selected such that their cluster correlations approach the expected values for a completely random arrangement of atoms.[40] Previous work has shown that SQSs can accurately replicate the experimental properties of disordered materials that approach the random limit owing to high configurational entropy.[10] In this work, each SQS was generated using a 5 × 6 × 8 supercell containing 480 atoms in its basis, matching the size of the largest structure sampled from our MC simulations. To inspect displacive SRO (i.e., changes in bond lengths) that may occur in the random configuration, these SQSs were relaxed using DFT calculations as described in the next section. Table 1 summarizes all the different models used in this work to model various aspects of SRO in LMTOF and LMNTOF based on their PDFs.

Table 1. Summary of the Methods Used to Model the Neutron PDFs in This Work[a]

model	SRO
average structure	none
relaxed SQS	displacive
fixed-lattice MC	configurational
relaxed MC	both

[a]These are categorized by the type(s) of SRO they account for.

DFT Calculations. All 280 structures obtained from the MC simulations, as well as the SQS for each composition, were relaxed using first-principles computations performed with the Vienna ab initio simulation package.[41−44] Two different functionals were tested, including GGA + U[45] and SCAN.[46] In the former case, a Hubbard U-value of 3.9 eV was applied to the Mn ions in each structure.[47] All calculations were performed using the projector augmented wave method, where a cutoff energy of 600 eV was imposed on the plane wave basis sets. The Brillouin zone was sampled with Gaussian smearing (0.05 eV width) on a Γ-centered mesh containing at least 25 k-points per Å^{-1}. Atomic positions were relaxed until all forces were less than 10^{-2} eV/Å. We tested two different approaches to structural relaxation: (1) atomic positions were optimized while the unit cells were kept fixed to match the experimental lattice parameters and (2) lattice parameters and atomic positions were both optimized.

As detailed in Supporting Information, Note 1 and shown by the results given in Supporting Information, Figure S1, the SCAN functional consistently produced structures that most accurately represented the experimental PDF of each DRX composition. The use of GGA + U, on the other hand, failed to capture subtle distortions in the bond lengths caused by Jahn−Teller distortions, which significantly influence the PDF. We also found that the complete relaxation of the unit cell and atomic positions gave better results than calculations performed using a fixed cell. Because relaxation can sometimes introduce anisotropy in the supercell shapes, owing to their finite size, the relaxed lattice parameters were allowed to vary during refinement. Larger supercells generally showed better agreement with the experimental data, though the effect is small. Given that the best fit (minimal R_w) remains unchanged across the last three distributions based on incrementally larger unit cells (containing 320, 400, and 480 atoms), we suspect that the structures used in this work are sufficiently large to model the PDF data at hand. Based on these results, all structures discussed throughout the Results sections rely on a 5 × 6 × 8 supercell containing 480 atoms in its basis, where both the unit cell and atomic positions were relaxed using the SCAN functional.
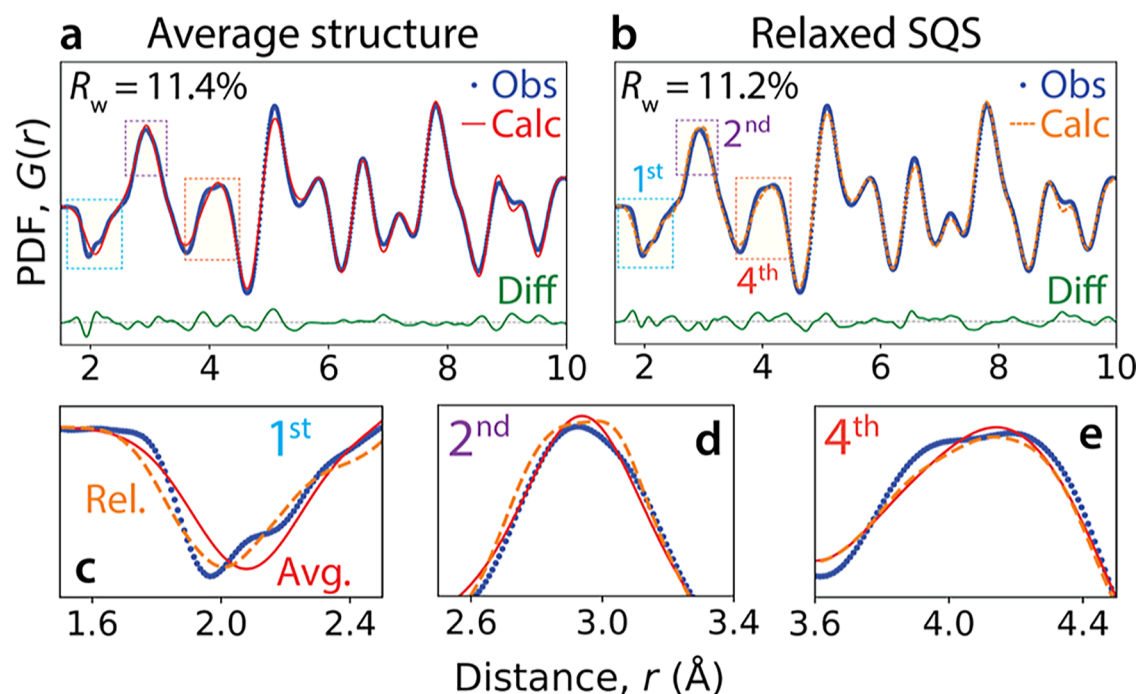
Figure 1. Neutron PDF analysis based on random ionic configurations. (a) Refinement performed using an average structure where all atoms occupy ideal positions on the fcc lattice. (b) Refinement of an SQS relaxed with DFT calculations. Blue dots represent experimental data (Obs) and red/orange lines represent calculated values (Calc). Green lines represent the difference between these two (Diff). Panels (c−e) show enlargements around the first three peaks where calculations and experiments differ most. In all cases, $G(r)$ is plotted in terms of Å^{-2}.

RESULTS

Structure Refinement Based on Random Site Occupancies. LMTOF was successfully synthesized without any detectable impurities, as illustrated by its diffraction pattern (Supporting Information, Figure S2). The positions and intensities of the measured peaks agree well with the average structure representing LMTOF (without any SRO), though some diffuse signal exists, which will modify several peaks in the PDF. By refining the average structure to the measured diffraction pattern (R_w = 4.1%), a lattice parameter of 4.15 Å is obtained. For all subsequent analysis, LMTOF is assumed to be a homogeneous solid solution in which the site occupancies lack any LRO but may possess some SRO, for which we estimate a coherence length of 9 Å by applying the Scherrer equation to the diffuse scattering in the diffraction pattern.[48] While some recent work suggests that disordered rocksalt materials synthesized by mechanochemistry may be composed of mixed domains,[49] the samples considered in this work were prepared by solid-state synthesis and are much more likely to be single phase. In contrast to materials prepared by mechanochemistry, which can be difficult to refine owing to the broad diffraction peaks they produce, LMTOF gives narrow diffraction peaks, suggesting good crystallinity and a large coherence length of the LRO features.

Figure 1a shows the calculated PDF (red line) for LMTOF based on its average structure, as refined to the experimental neutron data (blue dots). This model accurately represents the experimental PDF at large distances (Supporting Information, Figure S3) but fails to reproduce many of the features observed in the first four peaks that span $r < 5$ Å. For example, in the average structure, the first peak is found at too large a distance

(2.0 vs 1.97 Å), suggesting that SRO leads to changes in the nearest-neighbor (NN) bond lengths of LMTOF. This effect is further illustrated by the asymmetry observed in the first peak of the experimental PDF, which shows some degree of splitting that produces a small shoulder at ∼2.15 Å. More prominent splitting is also observed in the fourth peak of the experimental PDF, which contains two distinct maxima at 4.0 and 4.2 Å. In contrast, the fourth peak calculated using the average structures displays only one maximum at 4.14 Å, corresponding to the length of the anion−cation−anion connections (e.g., O−TM−O) spanning the octahedral complexes in LMTOF. Because the average structural model fails to reproduce these features, a large value of R_w = 11.4% is obtained from the refinement.

To account for displacive SRO while maintaining near-random site occupancies, refinement was also performed using the relaxed SQS for LMTOF. The corresponding results are shown in Figure 1b, where the calculated (dashed orange) and experimental (blue dots) PDFs are compared. Several noticeable changes in the PDF occur when displacive SRO is considered. As illustrated by the inset (Figure 1c), the calculated position of the first peak (2.01 Å) better matches the experimentally observed value (1.97 Å). This change in position can be traced back to the presence of shortened bonds surrounding the smaller Mn^{3+} (64.5 pm) and Ti^{4+} (60.5 pm) ions, as compared to the larger Li^+ (76 pm) ions that are most prominent in the average composition. Despite the improved representation of the first peak, the relaxed SQS still fails to reproduce much of the splitting that is observed experimentally, suggesting that configurational SRO may be needed to capture these features. Similar results are obtained for the fourth peak, as highlighted by the inset shown in Figure 1e.

The structural relaxations present in the SQS produce slightly increased asymmetry in this peak relative to the average structure, improving its agreement with the experimental data. From inspection of the SQS, we find that the observed splitting of the fourth peak is largely caused by Jahn−Teller distortions surrounding the Mn^{3+} ions in LMTOF, which result in the formation of four short equatorial bonds and two long axial bonds (details in cation−anion correlations). However, only some of the Mn^{3+} complexes in the SQS exhibit such distortions, and therefore, the splitting of the fourth peak (as well as the first) is weaker than observed in the experimental PDF. In the next section, we will discuss how configurational SRO is needed to facilitate an increased number of Jahn−Teller distortions and therefore accurately reproduce the experimental PDF.

The behavior of the second peak in the PDF is unique as it becomes less accurately modeled when displacive SRO is accounted for. As shown by Figure 1d, the relaxed SQS incorrectly predicts asymmetry in this peak, such that two shoulders are observed on either side of the experimental maximum. In contrast, the average structure produces a unimodal peak at $r \approx 2.93$ Å, closely matching the position of the experimental peak (2.92 Å). We attribute this effect to electrostatic repulsion between high-valent cations (Mn^{3+} and Ti^{4+}), which tend to relax away from one another when their octahedra are edge-sharing. Configurational SRO, however, can reduce the mixing between these species and therefore lessen their repulsion, as will be detailed in a later section (cation−cation correlations). Because the relaxed SQS provides a poor model for this peak but still gives improved accuracy for all other peaks at $r < 5$ Å, it results in a slightly better fit overall ($R_w = 11.2\%$) relative to the average structure model ($R_w = 11.4\%$).

Structure Refinement with Configurational SRO. To separate the effect of configurational SRO from that of the displacements it causes, PDFs were calculated based on the fixed-lattice MC structures where all ions occupy ideal positions in the fcc lattice. These simulated PDFs are shown in Supporting Information, Figure S4a alongside the experimental PDF for LMTOF. Interestingly, all 140 PDFs from the fixed-lattice MC structures are nearly identical to those obtained from the average structure model described in the previous section, with only slight variations in their relative peak intensities despite the fact that they possess configurational SRO. The refinements performed using these structures produced an average R_w of 11.4% with a standard deviation of only 0.1% across all 140 configurations sampled. In the absence of atomic displacements, the negligible influence of configurational SRO on the features of the PDF can in part be attributed to the similarity of O and F's neutron scattering lengths ($b_O = 5.803$ fm vs $b_F = 5.654$ fm).[35] This means that on a fixed lattice, any differences between the NN coordination environments of O and F will have little effect on the magnitude of each peak in the corresponding PDF.

In a second approach, the MC structures possessing configurational SRO were relaxed with DFT to account for the atomic displacements that took place. The PDFs calculated from these relaxed structures provide much better agreement with the experimental data obtained from LMTOF (Supporting Information, Figure S4b), resulting in fits that yield $R_w = 9.3\%$ on average. There is also much greater variation across PDFs calculated using different configurations when displacive SRO is accounted for. Refinements performed using the

relaxed MC structures gave a broad distribution of R_w with a standard deviation of 1.3%. Such variations can be traced to the stochastic nature of the MC simulations, which sample many different configurations with diverse coordination environments. For example, the average number of Li ions neighboring F ranges from 4.8 to 5.7 in the 140 MC structures considered here (Figure S5). Similar variations are also observed in the next-NN coordination environments (Figure S6). Because the bond lengths surrounding a given ion will relax differently depending on its neighbors, these changes lead to substantial modifications of the PDF which cause R_w to fluctuate from structure to structure. Despite these fluctuations, 132 of the 140 configurations considered here gave an improved fit of the experimental PDF after being relaxed (Figure S4c).

To more clearly illustrate the improved accuracy of these models with an example, we show in Figure 2 the PDF
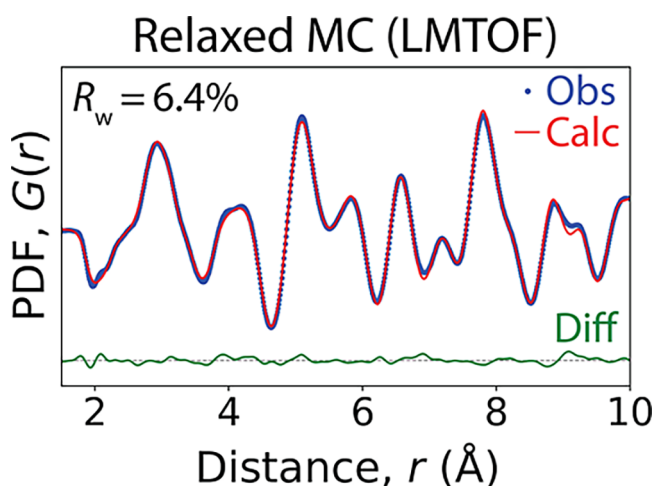

Figure 2. Refinement of the relaxed MC structure that best matches the experimental PDF for LMTOF. $G(r)$ is plotted in terms of Å^{-2}. Blue dots represent experimentally measured data (Obs) and red lines represent calculated values (Calc). Green lines represent their difference (Diff).

calculated from the relaxed MC structure that most closely reproduces the experimental data for LMTOF (i.e., gave a minimal R_w). Refinement based on this structure provides an excellent fit of the PDF with a low R_w of 6.4%, outperforming both the fixed-lattice MC structures ($R_w = 11.4\%$) and the relaxed SQS ($R_w = 11.2\%$) representing LMTOF. Much of the improvement occurs in the first few peaks at $r < 5$ Å, which are influenced by the coupling between configurational and displacive SRO as detailed in the next two sections. It should be noted that accurately modeling these features using the methods presented in this work requires a sufficiently large number of MC configurations to be sampled such that one with a low R_w can be identified.

In addition to accurately reproducing several key features of the PDF, the relaxed MC structure also maintains a good fit ($R_w = 4.1\%$) of the diffraction pattern shown in Supporting Information, Figure S7. In comparison to the average structure, the relaxed MC structure provides a more accurate model of the diffuse scattering associated with SRO, which appears in the calculated pattern as many small peaks whose combined profile resembles the experimentally observed features. The low intensities of these peaks highlight the importance of using

PDF measurements to analyze SRO. Whereas such features have a little influence on the refinement of the conventional diffraction pattern, they become more prominent in the PDF and therefore have a greater effect on its refinement, enabling a more detailed inspection of SRO.

Cation–Anion Correlations. To better understand the SRO observed in the LMTOF, we first consider how correlations between the cations (Li, Mn, and Ti) and anions (O, F) influence the first peak in the PDF, which is related to NN distances. Previous theoretical work has speculated that cation–anion correlations in DRX oxyfluorides are foremost influenced by a strong attraction between Li and F, which form a highly ionic bond that is energetically preferred over the TM-F bonds.[8,9,30] This prediction is supported by the experimental PDF presented here as the MC structure that most accurately reproduces it also reflects strong Li−F attraction. Figure 3
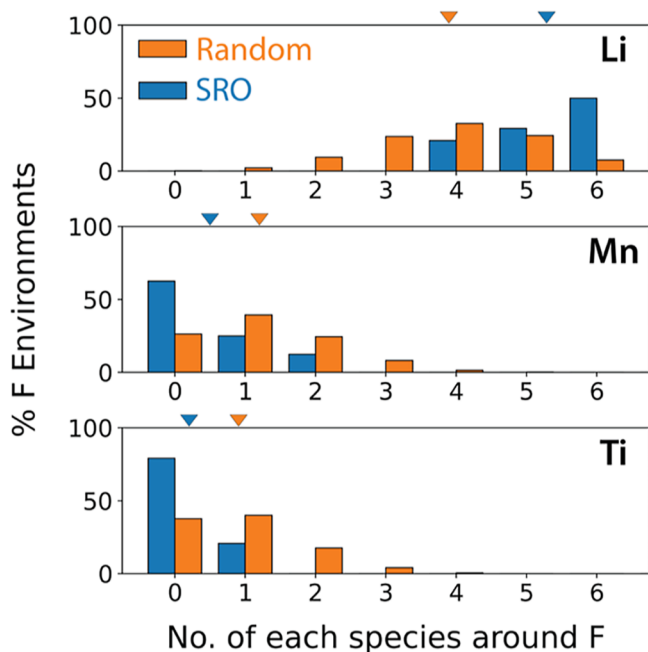

Figure 3. NN coordination environments of F ions in LMTOF. Each distribution represents the fraction of F environments (y-axis) with a given number of each cation species surrounding it (x-axis). These distributions are calculated for the MC structure (blue) that best matches the experimental PDF as well as for a random configuration (orange). Colored triangles at the top of each plot represent the average number of each species neighboring F.

shows the number of each cation species surrounding F ions within the MC structure possessing SRO. Indeed, each F is on average coordinated by ~5.3 Li ions, as compared to ~3.9 Li in a completely random configuration. This Li−F gettering effect leads to reduced bonding between each TM and F, and as a result, only 37% of all Mn ions (and 21% of Ti ions) are coordinated by ≥1 F ligands in the MC structure.

The coordination environments of Mn and F have a noticeable influence on their associated bond lengths. In cases where Mn is completely coordinated by O ligands, the MnO_6 octahedra undergo clear Jahn−Teller distortions,[50] resulting in four short equatorial bonds and two long axial bonds. On the other hand, when Mn is coordinated by at least one F ligand, less splitting of the surrounding bond lengths is observed. This is illustrated in Figure 4a, which shows the distribution of bond
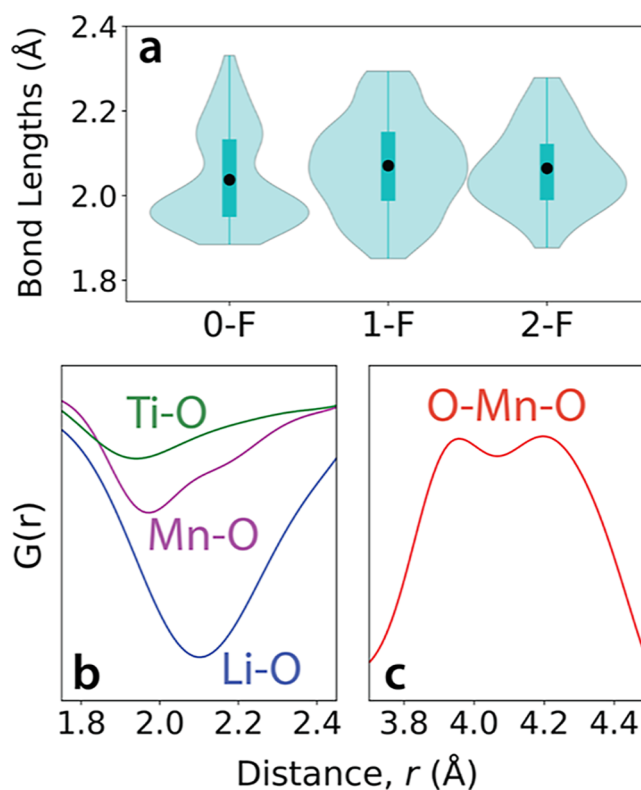

Figure 4. (a) Distributions of bond lengths in Mn octahedra coordinated by 0-F, 1-F, and 2-F. (b) Partial PDFs around the first peak representing NN bonds in the representative MC structure for LMTOF. (c) Partial PDF around the fourth peak representing O−Mn−O bonds that undergo Jahn−Teller distortions.

lengths around Mn ions coordinated only by O ligands (denoted 0-F), as compared with those coordinated by ≥1 F ligands (denoted 1-F and 2-F). The 0-F distribution is clearly bimodal, with two groups of bond lengths observed near 1.97 and 2.14 Å. In contrast, the 1-F and 2-F distributions become increasingly unimodal as more F ligands are introduced, suggesting weakened Jahn−Teller effects in such complexes.[37] We suspect that the mixture of O and F ligands surrounding Mn lifts the degeneracy of its e_g orbitals and therefore lessens the need for Jahn−Teller distortions. This is supported by previous experimental work on DRX oxyfluorides with compositions $Li_{1.2}Mn^{3+}_{0.6+0.5x}Nb^{5+}_{0.2-0.5x}O_{2-x}F_x$ (x = 0, 0.05, 0.1, 0.15, and 0.2). Analysis of their extended X-ray absorption fine structure data revealed that the heavily fluorinated samples possessed more uniform distributions of NN bond lengths (i.e., less Jahn−Teller distortions) as compared to the oxide sample.[37]

Because the MC simulations reported in this work predict that many of the Mn ions (~63%) in LMTOF are coordinated only by 0-F, the resulting structures display a substantial number of Jahn−Teller distortions to lift the degeneracy of the Mn e_g orbitals. This creates an increased number of short Mn−O bonds with an average length of 1.97 Å. Figure 4b shows the first peak of the partial PDFs calculated from the MC structure that best matches the experimental PDF, which reveals a low-r shoulder associated with the short equatorial Mn−O bonds in distorted MnO_6 octahedra. This effect, in addition to the presence of short Ti−O bonds, is critical to reproduce the position of the first peak in the experimental PDF (Figure 1c). Moreover, Jahn−Teller distortions are needed to account for
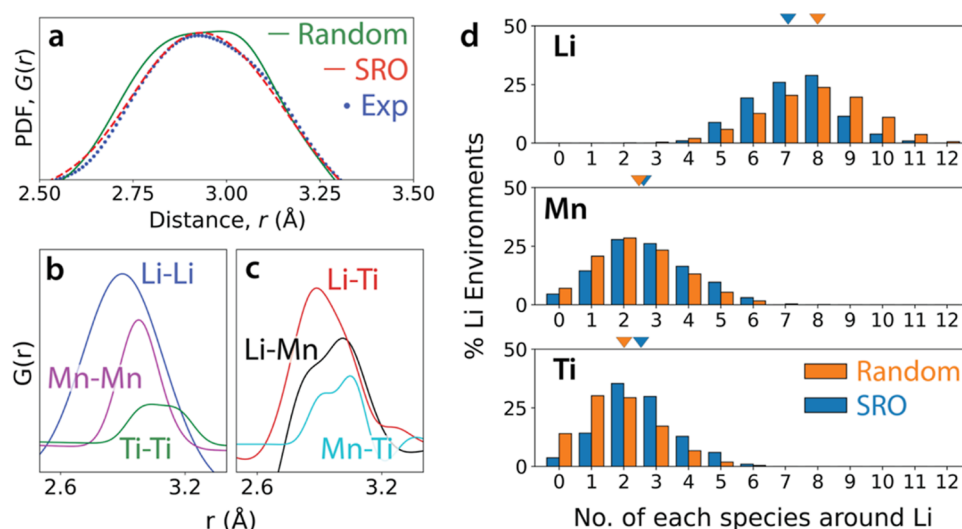
Figure 5. (a) The second peak of the PDF, which accounts for next-NN bonds, is plotted for LMTOF. Blue dots represent experimental data (Exp). The green line represents the PDF calculated from a relaxed SQS, whereas the red dashed is calculated from the relaxed MC structure that best matches experimental data. (b,c) Partial PDFs showing different cation−cation distances in the MC structure. (d) Distributions of Li's next-NN coordination environments for the MC structure (blue) vs a random configuration (orange). Colored triangles at the top of each plot represent the average number of each species neighboring Li.

the splitting observed in the fourth peak of the experimental PDF. Figure 4c shows the partial O−Mn−O PDF calculated using the representative MC structure, which correctly displays two clear maxima that agree well with the shape of the fourth peak in the experimental PDF (Figure 1e).

The analysis presented here demonstrates that while O and F cannot easily be distinguished by their neutron scattering lengths, their coordination environments can still be determined by assessing the influence of each anion on its neighboring bond lengths. Whereas scattering lengths affect the magnitude of each peak in the PDF, bond lengths set their positions. For materials containing a wide range of bond lengths, their PDFs are likely to contain several asymmetric and multi-modal peaks that reveal key information regarding the abundance of different bond pairs. LMTOF exemplifies this phenomenon, as the bimodal nature of the first peak in its PDF can only be reproduced by structures that have a minimal number of Mn−F bonds. Because MnO_6 octahedra display prominent Jahn−Teller distortions whereas octahedra containing F do not, structures with varied Mn−O/F coordination can be clearly distinguished and fit to the experimental PDF without requiring a detailed inspection of their scattering lengths.

In addition to the presence of Jahn−Teller distortions surrounding Mn^{3+}, there is the possibility of second-order Jahn−Teller distortions around Ti^{4+} as these sometimes occur in octahedral complexes containing d^0 transition metals.[51−53] Indeed, the distribution of bond lengths surrounding Ti^{4+} ions in LMTOF (Supporting Information, Figure S8) appears bimodal in complexes coordinated only by 0-F; however, the splitting of bond lengths observed around Ti^{4+} is much less prominent than for those around Mn^{3+} (Figure 3a). Second-order Jahn−Teller are often weaker than those of the first order, and Ti^{4+} in particular is considered to be the weakest distorter of all the common d^0 ions (e.g., compared to Zr^{4+}, Hf^{4+}, V^{5+}, Nb^{5+}, and Ta^{5+}).[52] Owing to the reduced magnitude of the Ti^{4+} displacements as well as the lower concentration of Ti^{4+} relative to that of Mn^{3+}, the suspected second-order Jahn−Teller distortions in LMTOF have a little effect on its

PDF, though we note that such distortions could play a larger role in compounds where the concentration of the d^0 element is increased.

Cation−Cation Correlations. Correlations among the cations (Li, Mn, and Ti) in LMTOF can also have a significant influence on its PDF. We study these by focusing on the second peak, which corresponds to next-NN distances representing the separation between metal centers in edge-sharing octahedra. Figure 5a shows the second peak of the PDF for LMTOF refined using two different models: the relaxed SQS (displacive SRO only) and the relaxed MC structure (configurational and displacive SRO) that best matches the experimental data. While the MC structure generates a unimodal peak that closely matches the experimental curve, the peak calculated from the SQS is strongly asymmetric with two shoulders on either side of the experimentally observed maximum. To further inspect this asymmetry, we plot in Figure 5b the partial PDFs of each cation pair in the relaxed MC structure. The peak positions in the partial PDFs reveal that the Mn−Mn and Ti−Ti distances are much larger than the Li−Li ones, which reflect strong electrostatic repulsion between the high-valent cations (Mn^{3+}, Ti^{4+}) in LMTOF. The fact that these different next-NN bond lengths are not properly weighed in a structure without SRO leads to a strong asymmetry in the second peak and consequently produces a poor fit of the experimental PDF. The MC structure, on the other hand, shows less asymmetry in this peak and therefore accurately reproduces the experimental curve. The enhanced symmetry in the second peak alludes to a more uniform distribution of next-NN bond lengths, which we attribute to the presence of configurational SRO that enables more intimate mixing between Li/Mn and Li/Ti (Figure 5c). These correlations minimize electrostatic repulsion by reducing the population of high-valent cations that neighbor one another, allowing the metal centers to remain more symmetric in their octahedral complexes.

Direct evidence of increased Li/TM mixing is given by the analysis of Li's next-NN coordination environment in the relaxed MC structure that best represents LMTOF. Figure 5d
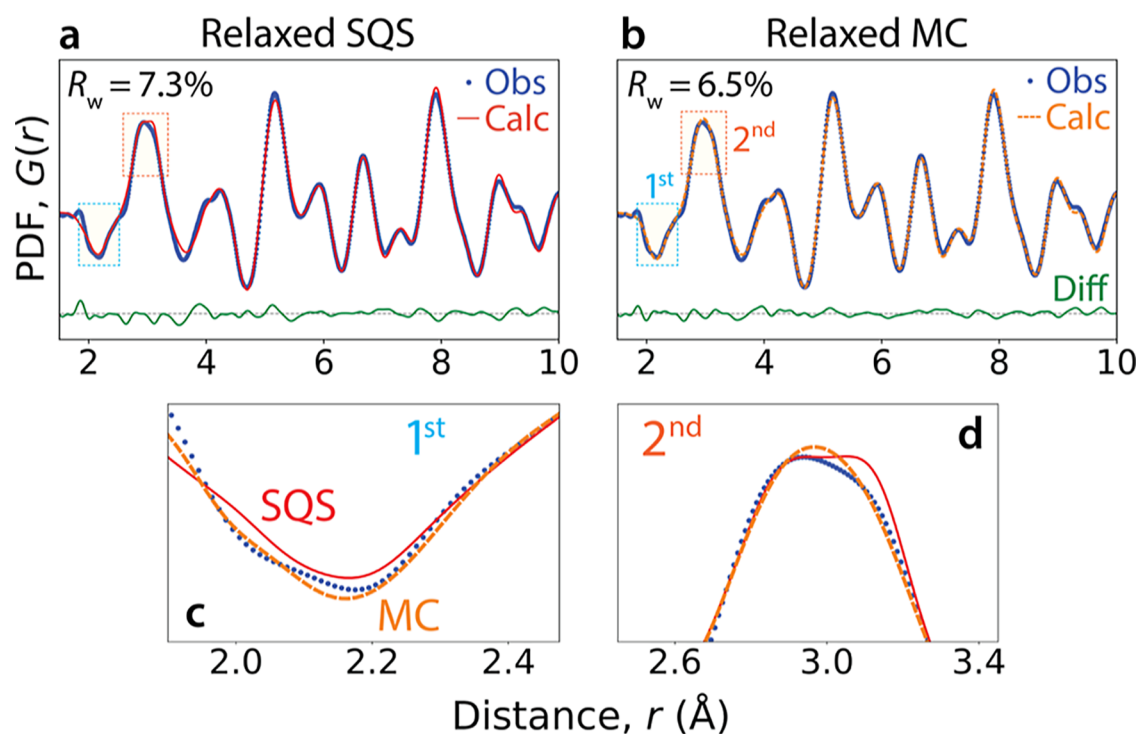
G

Figure 6. (a) Refinement of a relaxed SQS against experimental neutron PDF data for LMNTOF. (b) Refinement of the relaxed MC structure that best matches the experimental PDF. Blue dots represent experimental data (Obs) and red/orange lines represent calculated values (Calc). Green lines represent the difference between these two (Diff). Panels (c,d) show enlargements around the first two peaks. In all cases, $G(r)$ is plotted in terms of Å^{-2}.

shows the number of each cation species surrounding Li sites in the MC structure which accounts for configurational SRO, as well as for the equivalent sites in a completely random configuration. Configurational SRO leads to a reduced number of edge-sharing Li ions such that each Li in the MC structure is on average neighbored by only 7.1 Li, as opposed to 8.0 in the random configuration. In contrast, a large increase is observed in the number of edge-sharing Li−Ti octahedra due to SRO. Li ions in the MC structure have on average 2.5 Ti neighbors, as opposed to 2.0 in the random configuration. Similarly, a slight increase in Li−Mn coordination occurs, though to a lesser extent than Li−Ti. These results suggest that Li$^+$ tends to mix intimately with Ti^{4+} to create local electroneutrality, confirming the predictions reported in past computational work.[6] Here, we find that Li/Ti mixing is not only thermodynamically favored from a theoretical standpoint but also necessary to obtain an accurate fit of the experimental PDF.

Influence of Nb. All results discussed in the previous sections focus on the modeling of LMTOF, in which all Mn ions adopt a nominal +3 oxidation state and are therefore prone to Jahn−Teller distortions that cause prominent splitting in the first and fourth peaks of the corresponding PDF (see cation−anion correlations). In contrast, LMNTOF includes high-valent Nb^{5+} ions that lead to a reduced Mn oxidation state. Only 50% of Mn ions are expected to adopt the Jahn−Teller active +3 oxidation state in LMNTOF, and therefore, this composition may be used to probe the effects of SRO in materials where first-order Jahn−Teller distortions are less pronounced. The choice of Nb as a high-valent charge compensator was also inspired by previous work where several

Mn/Nb-based DRX cathodes were found to exhibit promising electrochemical performance.[54−56]

The diffraction pattern from LMNTOF indicates a successful synthesis without any detectable impurities (Supporting Information, Figure S9). Its refinement (R_w = 3.8%) based on an average structural model yields a lattice parameter of 4.22 Å, suggesting a slight expansion relative to LMTOF (4.15 Å) which is likely caused by the introduction of reduced Mn^{2+} ions (83 pm) and a decreased abundance of Mn^{3+} ions (64.5 pm). While the average structure provides a good fit of the narrow diffraction peaks derived from LRO, there also appears some diffuse scattering related to SRO (e.g., near a d-spacing of 1.15 Å), which is not accounted for by the average structural model. In comparison to LMTOF, the diffuse scattering observed from LMNTOF is less prominent, suggesting an increased level of disorder in this compound. Indeed, the coherence length of SRO calculated from the diffuse scattering is only 6 Å for LMNTOF, shorter than the calculated coherence length of 9 Å for LMTOF.

In Figure 6a, we show the neutron PDF of LMNTOF with refinement performed using a relaxed SQS that accounts for displacive SRO while maintaining a near-random distribution of site occupancies. In contrast to LMTOF, where the SQS provided a poor model of the experimental PDF (R_w = 11.2%), the SQS representing LMNTOF gives a much better fit (R_w = 7.3%). A key difference between these two compositions is illustrated by the first peak of the PDF shown in Figure 6c. Whereas LMTOF displayed splitting of this peak that resulted in a prominent shoulder at low distances ($r \approx 1.97$ Å), the first peak of LMNTOF displays a larger shoulder at high distances ($r \approx 2.17$ Å). This difference can be rationalized by the origin

of the peak splitting in each material. The low-r shoulder in LMTOF arises from the four short equatorial bonds in Mn^{3+} complexes with Jahn−Teller distortions. This effect is weaker in LMNTOF since it contains less Jahn−Teller active Mn^{3+} ions. Instead, a high-r shoulder appears due to local relaxations in bonds surrounding the large Mn^{2+} ions (83 pm). We stress that these relaxations will occur regardless of the neighboring sites, and therefore, the displacive SRO that causes asymmetry in the first peak of the PDF will be present even without any configurational SRO. Consequently, the relaxed SQS provides a reasonably accurate model of the first peak in the experimental PDF for LMNTOF.

In contrast to the first peak, the second peak of the PDF remains poorly fit by the relaxed SQS representing LMNTOF. As shown in Figure 6d, the PDF calculated from the SQS displays a second peak with strong asymmetry and a large shoulder at a distance (r) much higher than the experimentally observed maximum. This observation further supports our previous conclusions regarding the influence of configurational SRO (or lack thereof) on the shape of the second PDF peak. Because the relaxed SQS contains many edge-sharing high-valent cations (e.g., Ti^{4+} and Nb^{5+}), which tend to relax away from one another due to electrostatic repulsion, it results in a larger-than-expected next-NN bond length. Configurational SRO is therefore needed to reduce mixing between these high-valent cations, lessen their electrostatic repulsion, and produce a unimodal peak that better matches the experimental data.

To probe the effects of configurational SRO without considering its influence on the atomic displacements that take place, the fixed-lattice MC configurations representing LMNTOF were refined to their experimental PDF. The corresponding spectra show very little variation, producing relatively poor fits with an average R_w of 13.4% and a standard deviation of only 0.1%. In contrast, when configurational and displacive SRO are both accounted for by relaxing the MC structures, their PDFs show improved agreement with the experimental data. The distribution of R_w obtained from refining the relaxed structures representing LMNTOF has a mean of 9.7% and a standard deviation of 1.7% (Supporting Information, Figure S10). This suggests increased variance in the spectra as compared to LMTOF, where the standard deviation in R_w is 1.3%, which we suspect originates from the additional degrees of freedom introduced by including Nb in the composition. The increased number of elements, as well as the newly mixed Mn^{2+}/Mn^{3+} oxidation states, leads to a greater number of configurations that can be sampled by the MC simulations. These different configurations subsequently affect the bond length relaxations that take place, which affect several features in the PDF as detailed below.

Supporting Information, Figure S11 shows the distributions of NN coordination environments surrounding F in all 140 MC configurations representing LMNTOF. In contrast to LMTOF (Figure S5), which had a relatively uniform distribution of coordination environments, there appear two distinct groups of configurations for LMNTOF. One of these groups contains F ions that are heavily coordinated by Li, appearing similar to LMTOF, whereas the other group shows less Li−F coordination and instead has an increased number of Mn−F bonds. This dichotomy is more clearly illustrated by the scatter plots in Figure S12, where each dot represents the average number of Li and Mn ions neighboring F in a single MC configuration. A group of outliers possessing increased Mn−F coordination is highlighted in red. The existence of

these configurations suggests that Mn^{2+} is more likely to bond with F than Mn^{3+}, requiring a lower energy cost and therefore appearing more often in the MC simulations. This is supported by the previous work of Ouyang et al.,[8] which showed that Mn^{2+}-based DRX compositions generally have higher F solubility than their Mn^{3+}-based counterparts. Next-NN interactions may also play some role in creating different configurations for LMNTOF. As shown in Figures S13 and S14, there exists a group of LMNTOF configurations with increased Li/Mn coordination relative to LMTOF. We suspect this is caused by the introduction of Mn^{2+} (83 pm), which tends to mix more intimately with Li^+ (76 pm) owing to their similar ionic radii—both of which are much larger than Mn^{3+} (64.5 pm), Ti^{4+} (60.5 pm), and Nb^{5+} (64 pm).[6]

Figure 6b shows the refinement of LMNTOF performed using the PDF that was calculated using the relaxed MC structure that best reproduces the experimental curve. By accounting for both configurational and displacive SRO, this model gives an improved fit (R_w = 6.5%) over the relaxed SQS (R_w = 7.3%). The MC structure also maintains a good fit with the conventional diffraction pattern (R_w = 3.8%, Supporting Information, Figure S15), reproducing the experimental peaks while also accounting for the diffuse scattering that dictates the appearance of the PDF. The most noticeable difference between the SQS and the MC structure occurs in the second peak of the PDF (Figure 6d), where the MC structure correctly predicts a symmetric and unimodal curve that closely resembles the experimental peak with a maximum at $r \approx 2.94$ Å. The disappearance of the high-r shoulder upon including configurational SRO is caused by the more intimate mixing that takes place between Li and the high-valent TMs (Mn^{3+}, Ti^{4+}, and Nb^{5+}), similar to the effect discussed in cation−cation correlations and illustrated by the average Li coordination environments in Supporting Information, Figure S16. Another, less noticeable, difference between the PDFs produced by the MC structure versus the SQS is observed in the first peak (Figure 6c), related to NN interactions. The first peak calculated using the MC structure shows slightly increased splitting, such that the left shoulder near $r \approx 2.01$ Å appears more prominent. We suspect this difference arises from an increased number of Jahn−Teller distortions associated with $Mn^{3+}-O_6$ octahedra, as configurational SRO between the cations and anions in LMNTOF favors Li−F over Mn−F bonds (Supporting Information, Figure S17). This finding reflects our previous results from LMTOF; however, the effect is less prominent due to a reduced proportion of Jahn−Teller active Mn^{3+} ions in LMNTOF.

While the first-order Jahn−Teller distortions associated with Mn are effectively reduced in LMNTOF, the second-order Jahn−Teller effects associated with the d^0 elements may become more pronounced owing to the introduction of Nb^{5+}. In contrast to Ti^{4+}, this cation has a higher electronegativity and more diffuse t_{2g} orbitals which can hybridize with the neighboring O 2p orbitals, and consequently, larger off-center displacements are often observed in Nb-containing octahedra.[51,52] A similar trend is identified here as the distribution of bond lengths surrounding Nb^{5+} ions in LMNTOF shows bimodal splitting that is much more pronounced than that observed for the Ti^{4+} ions (Supporting Information, Figure S8). Nevertheless, considering that Nb accounts for only 5% of all the cations in LMNTOF, its effect on the PDF remains small. To illustrate this, a comparison can be made between the partial PDFs of each bond pair in Supporting Information,
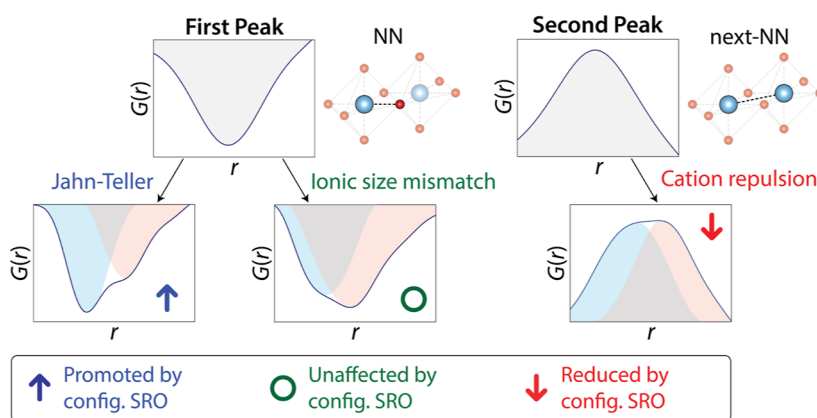
Figure 7. Summary of the three major factors that dictate the appearance of neutron PDFs from Mn^{3+}-based DRX oxyfluorides. These factors are categorized by their effects on the first peak, related to NN distances, and the second peak, related to next-NN distances. Shading is used to emphasize the different modes in each peak. Also shown is the influence of configurational SRO on the prominence of each factor.
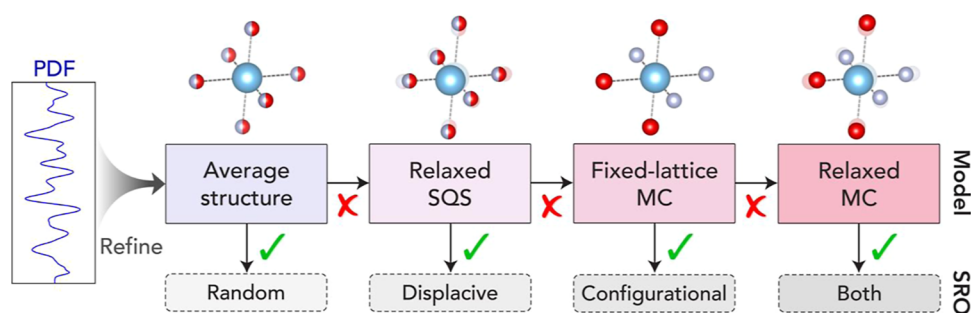

Figure 8. Outline of the four different models used to refine SRO structures based on PDF fitting, ordered in terms of increasing complexity (additional levels of SRO).

Figure S18, which reveals that the Nb−O and Ti−O curves have much weaker contributions to the overall PDF than the Li−O and Mn−O curves.

DISCUSSION

Our findings demonstrate that experimental PDFs can be accurately modeled using first-principles calculations. MC simulations on CEs provide an effective method to sample low-energy configurations that account for configurational SRO,[8] and these configurations can be relaxed with DFT to capture displacive SRO. Both effects are critical to reproduce the experimental PDFs obtained from the two DRX oxyfluorides studied in this work. Furthermore, configurational SRO and displacive SRO are strongly coupled, such that differences in site occupancies have a clear impact on the observed atomic displacements that take place, which in turn modify the shapes and positions of the first few peaks in the PDF of each material. Specifically, three factors were identified as critical components that must be accounted for to obtain accurate models of the experimental PDF data for LMTOF and LMNTOF. These factors are detailed below, and their influence on the first and second peaks of the PDF is illustrated in Figure 7.

1. Li−F correlation and its effect on Jahn−Teller distortions: octahedra containing Mn^{3+} tend to adopt Jahn−Teller distortions when fully coordinated by 0-F. This manifests itself in the PDF by causing the first peak to split into two distinct shoulders associated with the lengths of the short equatorial and long axial Mn−O bonds in each octahedron. The amount of splitting that takes place is related to configurational cation−anion

SRO. In particular, the increased Li−F coordination caused by SRO "steals" F ligands from Mn octahedra and ensures that their e_g orbitals remain degenerate, thus providing an incentive for the Jahn−Teller distortions to occur.

2. Cation mixing and electrostatic repulsion: high-valent cations such as Ti^{4+} and Nb^{5+} relax away from one another when they occupy edge-sharing octahedra. This causes the second peak in the PDF to become asymmetric, with a shoulder at high r associated with an increase in the next-NN distances. However, because configurational SRO favors the separation of these high-valent cations to reduce their electrostatic repulsion, the experimental PDFs avoid much of the expected asymmetry in the second peak.

3. Ionic size mismatch causing local displacements: when a disordered material contains ions with large differences in their radii, local displacements occur to minimize strain. This can lead to splitting in the first peak of the PDF, where each shoulder represents a distinct NN bond length in the various local coordination environments.

More generally, our analysis reveals that observed asymmetries in the peaks of a given PDF do not necessarily signify the presence of configurational SRO. Indeed, while factors (1) and (2) outlined above can be affected by SRO, factor (3) is present even in a material with a completely random distribution of site occupancies. This is because the average structure may not be an accurate representation of the *real* structure, regardless of whether it possesses configurational

SRO. Each site in a real disordered crystal can have a different set of chemical neighbors, which often leads to distinct bond lengths, especially when the material contains many ions with different radii. Since the PDF accounts for the local structure, not the average one, it reveals these differences in bond lengths through splitting or asymmetry in its peaks. Careful inspection of the PDF (e.g., by comparing different models) is necessary to discern whether these asymmetries arise from displacive SRO by itself or whether configurational SRO also plays a role.

In Figure 8, we outline a step-by-step workflow to model SRO in disordered crystalline materials by refining structural models generated from first-principles calculations to fit experimental PDF data. This workflow is applicable to X-ray and neutron PDF measurements, which each provide complementary information owing to the distinct interaction strength of different elements with X-rays versus neutrons, and these techniques may also be combined for multi-modal analysis.[57−59] After the PDF data is obtained, one may start with an average structural model based on a primitive unit cell. In materials that possess any SRO, this model should produce a poor fit to the experimental PDF data. To account for displacive SRO while maintaining near-random site occupancies, an SQS may be generated and relaxed using DFT. Should this model provide an accurate representation of the experimental PDF, it suggests that the corresponding material lacks configurational SRO but displays some variations in its local coordination environments (e.g., due to an ionic size mismatch). Alternatively, if the relaxed SQS is inaccurate, configurational SRO can be modeled using CE-based MC simulations to obtain low-energy distributions of site occupancies on a fixed lattice. If these MC accurately reproduce the experimental PDF, it signifies the presence of configurational SRO but a lack of displacive SRO. Such a case may occur in materials containing species with greatly differing scattering lengths but similar ionic radii. Last, if none of the aforementioned methods provide an accurate model of the experimental PDF, both configurational SRO and displacive SRO are needed. These effects can be accounted for by relaxing the MC structures with DFT calculations. As demonstrated here, relaxed MC structures are generally the most reliable models for experimental PDF data and can be used to pinpoint the origin of SRO by analyzing their corresponding site occupancies and atomic displacements.

CONCLUSIONS

We have tested a variety of techniques to model SRO in disordered crystalline materials using first-principles simulations. The accuracy of each method was validated on two DRX oxyfluorides, from which PDFs were collected using total neutron scattering measurements. Both PDFs contain several asymmetric and bimodal peaks at short distances ($r < 5$ Å), which deviate from the features expected for an average structure model with random site occupancies. We demonstrated that these deviations arise from changes in bond lengths associated with distinct local coordination environments, otherwise referred to as displacive SRO. To some extent, this can be modeled using a relaxed SQS, which accounts for local displacements while maintaining a near-random ionic configuration. However, to fully reproduce the experimental data, configurational SRO must also be considered as it indirectly influences the PDF by setting the local coordination environment of each species. Coupling between configurational and displacive SRO is accurately

modeled by structures sampled from MC simulations and relaxed using DFT, which gave the best agreement with the experimental data out of all the models considered in this work. These findings confirm the effectiveness of first-principles techniques as applied to the study of complex, multi-component systems with configurational disorder. By combining these methods with experimental characterization techniques such as PDF analysis, a precise and quantitative description of SRO can be obtained. This may lead to further development of disordered materials by enabling precise control over their SRO, which can be used to fine-tune their properties for applications such as Li-ion batteries.[6,8]

ASSOCIATED CONTENT

Ⓢ Supporting Information

The Supporting Information is available free of charge at https://pubs.acs.org/doi/10.1021/acs.chemmater.2c03827.

> Discussion regarding the choice of DFT functional and lattice constraints, conventional diffraction patterns, refined PDFs from all MC structures, and analysis of their coordination environments (PDF)

AUTHOR INFORMATION

Corresponding Authors

Bin Ouyang − *Department of Chem. & Biochemistry, Florida State University, Tallahassee, Florida 32306, United States*; Email: bouyang@fsu.edu

Gerbrand Ceder − *Department of Mat. Sci. & Engineering, UC Berkeley, Berkeley, California 94720, United States; Materials Sciences Division, Lawrence Berkeley National Laboratory, Berkeley, California 94720, United States*; ⓞ orcid.org/0000-0001-9275-3605; Email: gceder@berkeley.edu

Authors

Nathan J. Szymanski − *Department of Mat. Sci. & Engineering, UC Berkeley, Berkeley, California 94720, United States; Materials Sciences Division, Lawrence Berkeley National Laboratory, Berkeley, California 94720, United States*; ⓞ orcid.org/0000-0003-2255-9676

Zhengyan Lun − *School of Chemical Sciences, University of Chinese Academy of Sciences, Beijing 100049, China*

Jue Liu − *Neutron Scattering Division, Oak Ridge National Laboratory, Oak Ridge, Tennessee 37830, United States*; ⓞ orcid.org/0000-0002-4453-910X

Ethan C. Self − *Chemical Sciences Division, Oak Ridge National Laboratory, Oak Ridge, Tennessee 37830, United States*; ⓞ orcid.org/0000-0001-6006-6317

Christopher J. Bartel − *Department of Chem. Eng. & Mat. Sci., University of Minnesota, Minneapolis, Minnesota 55455, United States*; ⓞ orcid.org/0000-0002-5198-5036

Jagjit Nanda − *Applied Energy Division, SLAC National Laboratory, Menlo Park, California 94025, United States*

Complete contact information is available at:
https://pubs.acs.org/10.1021/acs.chemmater.2c03827

Notes

The authors declare no competing financial interest.

ACKNOWLEDGMENTS

■ REFERENCES

(1) Oses, C.; Toher, C.; Curtarolo, S. High-entropy ceramics. *Nat. Rev. Mater.* **2020**, *5*, 295−309.

(2) Leroux, M.; Mishra, V.; Ruff, J. P. C.; Claus, H.; Smylie, M. P.; Opagiste, C.; Rodière, P.; Kayani, A.; Gu, G. D.; Tranquada, J. M.; et al. Disorder raises the critical temperature of a cupratesuperconductor. *Proc. Natl. Acad. Sci. U.S.A.* **2019**, *116*, 10691−10697.

(3) O'Quinn, E. C.; Sickafus, K. E.; Ewing, R. C.; Baldinozzi, G.; Neuefeind, J. C.; Tucker, M. G.; Fuentes, A. F.; Drey, D.; Lang, M. K. Predicting short-range order and correlated phenomena in disordered crystalline materials. *Sci. Adv.* **2020**, *6*, No. eabc2758.

(4) Owen, L. R.; Playford, H.; Stone, H.; Tucker, M. Analysis of short-range order in Cu₃Au using X-ray pair distribution functions. *Acta Mater.* **2017**, *125*, 15−26.

(5) Proffen, T.; Petkov, V.; Billinge, S. J. L.; Vogt, T. Chemical short range order obtained from the atomic pair distribution function. *Z. Kristallogr.* **2002**, *217*, 47−50.

(6) Ji, H.; Urban, A.; Kitchaev, D. A.; Kwon, D. H.; Artrith, N.; Ophus, C.; Huang, W.; Cai, Z.; Shi, T.; Kim, J. C.; et al. Hidden structural and chemical order controls lithium transport in cation-disordered oxides for rechargeable batteries. *Nat. Commun.* **2019**, *10*, 592.

(7) Richards, W. D.; Dacek, S. T.; Kitchaev, D. A.; Ceder, G. Fluorination of Lithium-Excess Transition Metal Oxide Cathode Materials. *Adv. Energy Mater.* **2017**, *8*, 1701533.

(8) Ouyang, B.; Artrith, N.; Lun, Z.; Jadidi, Z.; Kitchaev, D. A.; Ji, H.; Urban, A.; Ceder, G. Effect of Fluorination on Lithium Transport and Short-Range Order in Disordered-Rocksalt-Type Lithium-Ion Battery Cathodes. *Adv. Energy Mater.* **2020**, *10*, 1903240.

(9) Lun, Z.; Ouyang, B.; Cai, Z.; Clément, R. J.; Kwon, D. H.; Huang, J.; Papp, J. K.; Balasubramanian, M.; Tian, Y.; McCloskey, B. D.; et al. Design Principles for High-Capacity Mn-Based Cation-Disordered Rocksalt Cathodes. *Chem* **2020**, *6*, 153−168.

(10) Lun, Z.; Ouyang, B.; Kwon, D. H.; Ha, Y.; Foley, E. E.; Huang, T. Y.; Cai, Z.; Kim, H.; Balasubramanian, M.; Sun, Y.; et al. Cation-disordered rocksalt-type high-entropy cathodes for Li-ion batteries. *Nat. Mater.* **2020**, *20*, 214−221.

(11) Cowley, J. M. X-Ray Measurement of Order in Single Crystals of Cu3Au. *J. Appl. Phys.* **1950**, *21*, 24−30.

(12) Moss, S. C. X-Ray Measurement of Short-Range Order in Cu3Au. *J. Appl. Phys.* **1964**, *35*, 3547−3553.

(13) Clapp, P. C.; Moss, S. C. Correlation Functions of Disordered Binary Alloys. I. *Phys. Rev. B: Condens. Matter Mater. Phys.* **1966**, *142*, 418−427.

(14) Billinge, S. J. L. The rise of the X-ray atomic pair distribution function method: a series of fortunate events. *Philos. Trans. R. Soc., A* **2019**, *377*, 20180413.

(15) Terban, M. W.; Billinge, S. J. L. Structural Analysis of Molecular Materials Using the Pair Distribution Function. *Chem. Rev.* **2022**, *122*, 1208−1272.

(16) Egami, T.; Billinge, S. *Underneath the Bragg Peaks: Structural Analysis of Complex Materials*; Elsevier: Amsterdam, The Netherlands, 2012.

(17) Rietveld, H. M. A profile refinement method for nuclear and magnetic structures. *J. Appl. Crystallogr.* **1969**, *2*, 65−71.

(18) Pawley, G. S. Unit-cell refinement from powder diffraction scans. *J. Appl. Crystallogr.* **1981**, *14*, 357−361.

(19) Le Bail, A.; Duroy, H.; Fourquet, J. L. Ab-initio structuredetermination of LiSbWO6 by X-ray powder diffraction. *Mater. Res. Bull.* **1988**, *23*, 447−452.

(20) McGreevy, R. L. Reverse Monte Carlo modelling. *J. Phys.: Condens. Matter* **2001**, *13*, R877−R913.

(21) Hui, Q.; Tucker, M. G.; Dove, M. T.; Wells, S. A.; Keen, D. A. Total scattering and reverse Monte Carlo study of the 105 K displacive phase transition in strontium titanate. *J. Phys.: Condens. Matter* **2005**, *17*, S111−S124.

(22) Tucker, M. G.; Keen, D. A.; Dove, M. T.; Goodwin, A. L.; Hui, Q. RMCProfile: reverse Monte Carlo for polycrystalline materials. *J. Phys.: Condens. Matter* **2007**, *19*, 335218.

(23) McGreevy, R. L. Reverse Monte Carlo: fact and fiction. *J. Non-Cryst. Solids* **1993**, *156−158*, 949−955.

(24) McGreevy, R. L.; Zetterström, P. To RMC or not to RMC? The use of reverse Monte Carlo modelling. *Curr. Opin. Solid State Mater. Sci.* **2003**, *7*, 41−47.

(25) Tucker, M. G.; Dove, M. T.; Keen, D. A. Application of the reverse Monte Carlo method to crystalline materials. *J. Appl. Crystallogr.* **2001**, *34*, 630−638.

(26) Tepesch, P. D.; Garbulsky, G. D.; Ceder, G. Model for Configurational Thermodynamics in Ionic Systems. *Phys. Rev. Lett.* **1995**, *74*, 2272−2275.

(27) Van der Ven, A.; Ceder, G. Vacancies in ordered and disordered binary alloys treated with the cluster expansion. *Phys. Rev. B: Condens. Matter Mater. Phys.* **2005**, *71*, 054102.

(28) Proffen, T. Analysis of occupational and displacive disorder using the atomic pair distribution function: a systematic investigation. *Z. Kristallogr.* **2000**, *215*, 661−668.

(29) Clément, R. J.; Lun, Z.; Ceder, G. Cation-disordered rocksalt transition metal oxides and oxyfluorides for high energy lithium-ion cathodes. *Energy Environ. Sci.* **2020**, *13*, 345−373.

(30) Kitchaev, D. A.; Lun, Z.; Richards, W. D.; Ji, H.; Clément, R. J.; Balasubramanian, M.; Kwon, D. H.; Dai, K.; Papp, J. K.; Lei, T.; et al. Design principles for high transition metal capacity in disordered rocksalt Li-ion cathodes. *Energy Environ. Sci.* **2018**, *11*, 2159−2171.

(31) Szymanski, N. J.; Zeng, Y.; Bennett, T.; Patil, S.; Keum, J. K.; Self, E. C.; Bai, J.; Cai, Z.; Giovine, R.; Ouyang, B.; et al. Understanding the Fluorination of Disordered Rocksalt Cathodes through Rational Exploration of Synthesis Pathways. *Chem. Mater.* **2022**, *34*, 7015−7028.

(32) Neuefeind, J.; Feygenson, M.; Carruth, J.; Hoffmann, R.; Chipley, K. K. The Nanoscale Ordered MAterials Diffractometer NOMAD at the Spallation Neutron Source SNS. *Nucl. Instrum. Methods Phys. Res., Sect. B* **2012**, *287*, 68−75.

(33) Calder, S.; An, K.; Boehler, R.; Dela Cruz, C. R.; Frontzek, M. D.; Guthrie, M.; Haberl, B.; Huq, A.; Kimber, S. A. J.; Liu, J.; et al. A suite-level review of the neutron powder diffraction instruments at Oak Ridge National Laboratory. *Rev. Sci. Instrum.* **2018**, *89*, 092701.

(34) Juhás, P.; Farrow, C.; Yang, X.; Knox, K.; Billinge, S. Complex modeling: a strategy and software program for combining multiple information sources to solve ill posed structure and nanostructure inverse problems. *Acta Crystallogr., Sect. A: Found. Adv.* **2015**, *71*, 562−568.

(35) Sears, V. F. Neutron scattering lengths and cross sections. *Neutrons News* **1992**, *3*, 26−37.

(36) Bellaiche, L.; Vanderbilt, D. Virtual crystal approximation revisited: Application to dielectric and piezoelectric properties of perovskites. *Phys. Rev. B: Condens. Matter Mater. Phys.* **2000**, *61*, 7877−7882.

(37) Lun, Z.; Ouyang, B.; Kitchaev, D. A.; Clément, R. J.; Papp, J. K.; Balasubramanian, M.; Tian, Y.; Lei, T.; Shi, T.; McCloskey, B. D.;

et al. Improved Cycling Performance of Li-Excess Cation-Disordered Cathode Materials upon Fluorine Substitution. *Adv. Energy Mater.* **2018**, *9*, 1802959.

(38) Nelson, L. J.; Hart, G. L. W.; Zhou, F.; Ozoliņš, V. Compressive sensing as a paradigm for building physics models. *Phys. Rev. B: Condens. Matter Mater. Phys.* **2013**, *87*, 035125.

(39) Chib, S.; Greenberg, E. Understanding the metropolis-hastings algorithm. *Am. Stat.* **1995**, *49*, 327−335.

(40) Zunger, A.; Wei, S. H.; Ferreira, L. G.; Bernard, J. E. Special quasirandom structures. *Phys. Rev. Lett.* **1990**, *65*, 353−356.

(41) Kresse, G.; Furthmüller, J. Efficiency of ab-initio total energy calculations for metals and semiconductors using a plane-wave basis set. *Comput. Mater. Sci.* **1996**, *6*, 15−50.

(42) Kresse, G.; Furthmüller, J. Efficient iterative schemes for ab initio total-energy calculations using a plane-wave basis set. *Phys. Rev. B: Condens. Matter Mater. Phys.* **1996**, *54*, 11169−11186.

(43) Kresse, G.; Hafner, J. Ab initio molecular dynamics for liquid metals. *Phys. Rev. B: Condens. Matter Mater. Phys.* **1993**, *47*, 558−561.

(44) Kresse, G.; Hafner, J. Ab initio molecular-dynamics simulation of the liquid-metal−amorphous-semiconductor transition in germanium. *Phys. Rev. B: Condens. Matter Mater. Phys.* **1994**, *49*, 14251−14269.

(45) Wang, L.; Maxisch, T.; Ceder, G. Oxidation energies of transition metal oxides within the GGA+U framework. *Phys. Rev. B: Condens. Matter Mater. Phys.* **2006**, *73*, 195107.

(46) Sun, J.; Ruzsinszky, A.; Perdew, J. P. Strongly Constrained and Appropriately Normed Semilocal Density Functional. *Phys. Rev. Lett.* **2015**, *115*, 036402.

(47) Jain, A.; Hautier, G.; Ong, S. P.; Moore, C. J.; Fischer, C. C.; Persson, K. A.; Ceder, G. Formation enthalpies by mixing GGA and GGA+U calculations. *Phys. Rev. B: Condens. Matter Mater. Phys.* **2011**, *84*, 045115.

(48) Patterson, A. L. The Scherrer Formula for X-Ray Particle Size Determination. *Phys. Rev.* **1939**, *56*, 978−982.

(49) Lee, E.; Wi, T.; Park, J.; Park, S.; Kim, M.; Lee, D.; Park, B.; Jo, C.; Malik, R.; Lee, J. H.; et al. Nanocomposite Engineering of a High-Capacity Partially Ordered Cathode for Li-ion Batteries. *Adv. Mater.* **2023**, *35*, 2208423.

(50) Arroyo y de Dompablo, M. E.; Marianetti, C.; Van der Ven, A.; Ceder, G. Jahn-Teller mediated ordering in layered LixMO2 compounds. *Phys. Rev. B: Condens. Matter Mater. Phys.* **2001**, *63*, 144107.

(51) Eng, H. W.; Barnes, P. W.; Auer, B. M.; Woodward, P. M. Investigations of the electronic structure of d0 transition metal oxides belonging to the perovskite family. *J. Solid State Chem.* **2003**, *175*, 94−109.

(52) Shiv Halasyamani, P. Asymmetric Cation Coordination in Oxide Materials: Influence of Lone-Pair Cations on the Intra-octahedral Distortion in d0 Transition Metals. *Chem. Mater.* **2004**, *35*, 3586−3592.

(53) Jacquet, Q.; et al. Electrostatic Interactions versus Second Order Jahn−Teller Distortion as the Source of Structural Diversity in Li3MO4 Compounds (M = Ru, Nb, Sb and Ta). *Chem. Mater.* **2018**, *30*, 392−402.

(54) Jones, M. A.; Reeves, P. J.; Seymour, I. D.; Cliffe, M. J.; Dutton, S. E.; Grey, C. P. Short-range ordering in a battery electrode, the 'cation-disordered' rocksalt $Li_{1.25}Nb_{0.25}Mn_{0.5}O_2$. *Chem. Commun.* **2019**, *55*, 9027−9030.

(55) Wang, R.; Li, X.; Liu, L.; Lee, J.; Seo, D. H.; Bo, S. H.; Urban, A.; Ceder, G. A disordered rock-salt Li-excess cathode material with high capacity and substantial oxygen redox activity: Li1.25Nb0.25Mn0.5O2. *Electrochem. Commun.* **2015**, *60*, 70−73.

(56) Yue, Y.; Li, N.; Li, L.; Foley, E. E.; Fu, Y.; Battaglia, V. S.; Clément, R. J.; Wang, C.; Tong, W. Redox Behaviors in a Li-Excess Cation-Disordered Mn−Nb−O−F Rocksalt Cathode. *Chem. Mater.* **2020**, *32*, 4490−4498.

(57) Aksel, E.; Forrester, J. S.; Nino, J. C.; Page, K.; Shoemaker, D. P.; Jones, J. L. Local atomic structure deviation from average structure of Na0.5Bi0.5TiO3: Combined x-ray and neutron total scattering study. *Phys. Rev. B: Condens. Matter Mater. Phys.* **2013**, *87*, 104113.

(58) Bréger, J.; Dupré, N.; Chupas, P. J.; Lee, P. L.; Proffen, T.; Parise, J. B.; Grey, C. P. Short- and Long-Range Order in the Positive Electrode Material, Li(NiMn)0.5O2: A Joint X-ray and Neutron Diffraction, Pair Distribution Function Analysis and NMR Study. *J. Am. Chem. Soc.* **2005**, *127*, 7529−7537.

(59) Coduri, M.; Brunelli, M.; Scavini, M.; Allieta, M.; Masala, P.; Capogna, L.; Fischer, H. E.; Ferrero, C. Rare Earth doped ceria: a combined X-ray and neutron pair distribution function study. *Z. Kristallogr.—Cryst. Mater.* **2012**, *227*, 272−279.

🔖 Recommended by ACS